

ORIGINAL RESEARCH

Open Access



# 3D printed anthropomorphic left ventricular myocardial phantom for nuclear medicine imaging applications

Janos Kiss<sup>1\*</sup>, Laszlo Balkay<sup>2</sup>, Kornel Kukuts<sup>3</sup>, Marton Miko<sup>2</sup>, Attila Forgacs<sup>3,4</sup>, Gyorgy Trencsenyi<sup>2</sup> and Aron K. Krizsan<sup>3</sup>

\*Correspondence:

kiss.janos31@med.unideb.hu

<sup>1</sup> Division of Radiology and Imaging Science, Department of Medical Imaging, Faculty of Medicine, University of Debrecen, Nagyerdei krt. 98., Debrecen 4032, Hungary  
Full list of author information is available at the end of the article

## Abstract

**Background:** Anthropomorphic torso phantoms, including a cardiac insert, are frequently used to investigate the imaging performance of SPECT and PET systems. These phantom solutions are generally featuring a simple anatomical representation of the heart. 3D printing technology paves the way to create cardiac phantoms with more complex volume definition. This study aimed to describe how a fillable left ventricular myocardium (LVm) phantom can be manufactured using geometry extracted from a patient image.

**Methods:** The LVm of a healthy subject was segmented from <sup>18</sup>F-FDG attenuation corrected PET image set. Two types of phantoms were created and 3D printed using polyethylene terephthalate glycol (PETG) material: one representing the original healthy LVm, and the other mimicking myocardium with a perfusion defect. The accuracy of the LVm phantom production was investigated by high-resolution CT scanning of 3 identical replicas. <sup>99m</sup>Tc SPECT acquisitions using local cardiac protocol were performed, without additional scattering media ("in air" measurements) for both phantom types. Furthermore, the healthy LVm phantom was inserted in the commercially available DataSpectrum Anthropomorphic Torso Phantom ("in torso" measurement) and measured with hot background and hot liver insert.

**Results:** Phantoms were easy to fill without any air-bubbles or leakage, were found to be reproducible and fully compatible with the torso phantom. Seventeen segments polar map analysis of the "in air" measurements revealed that a significant deficit in the distribution appeared where it was expected. 59% of polar map segments had less than 5% deviation for the "in torso" and "in air" measurement comparison. Excluding the deficit area, neither comparison had more than a 12.4% deviation. All the three polar maps showed similar apex and apical region values for all configurations.

**Conclusions:** Fillable anthropomorphic 3D printed phantom of LVm can be produced with high precision and reproducibility. The 3D printed LVm phantoms were found to be suitable for SPECT image quality tests during different imaging scenarios. The flexibility of the 3D printing process presented in this study provides scalable and anthropomorphic image quality phantoms in nuclear cardiology imaging.

**Keywords:** Cardiac, SPECT, 3D printing, Phantom, Technetium-99m

## Background

Performance measurements and optimization of nuclear medicine imaging systems involve the use of different phantoms to mimic human activity distributions [1–3]. Accurate anthropomorphic phantoms have been introduced to reveal quantitative inaccuracies and to detect the presence of image artefacts caused by inappropriate acquisition, reconstruction, and image processing [4–8]. Several of these phantoms are commercially available, generally with fixed size and geometry. 3D printing technology including direct ink writing [9], fused deposition modelling (FDM) [10–13], digital light processing (DLP) [14] or stereo-lithography (SLA) [15] offers large variety of possibilities to design custom-made geometrical and anthropomorphic phantoms [16–23]. A systematic review by Filippou et al. concludes that 3D printing methods can complete or replace commercially available phantoms in the fields of CT, MRI, PET, SPECT, US, and mammography imaging [24]. Several studies reveal 3D printed phantom solutions for nuclear medicine applications using real patient imaging data, including fillable multi-compartmental torso in quantitative imaging analysis for  $^{90}\text{Y}$ -DOTATATE radiopeptide therapy [25], fillable kidney phantom for  $^{177}\text{Lu}$  SPECT reconstruction optimization [26], as well as tumor phantom set of various shapes for testing comparison of PET radiomics features in a multi-center approach [27]. Focusing on cardiac phantom solutions, Matsutomo et al. designed and printed a set of specific inserts to simulate different ischemic levels to complete the commercially available Myocardial SPECT Phantom HL (Kyoto Kagaku Co., Ltd., Kyoto, Japan) [28]. Grice et al. introduced a left ventricle (LV) cardiac phantom with simplified wall geometry containing low perfusion lesions within a non-anthropomorphic background container, printed from polylactic acid (PLA) material [29]. The endeavor of creating new cardiac phantoms is encouraged by clinically relevant, but unanswered methodological questions. The lack of geometrically appropriate cardiac phantom prevents the investigation of image artefacts and image processing failures attributed to the inhomogeneity of the cardiac wall thickness. 3D printing technology makes it possible to create the complex geometry of a real heart, which is not feasible with traditional manufacturing methods. This study aimed to determine whether creating a fillable, anatomically accurate 3D printed left ventricle myocardium (LVm) phantom segmented from a PET image volume of a real patient is feasible. The suitability of polyethylene terephthalate glycol (PETG) plastic for anthropomorphic LVm phantom production is demonstrated for the first time. The phantom insert was designed to be compatible with the commercially available Anthropomorphic Torso Phantom (Data-Spectrum Co., Durham, NC). CT images are presented to confirm the reproducibility of 3D printing and phantom preparation. Furthermore, SPECT measurements were performed to demonstrate that the proposed phantoms give a complementary solution to the currently available phantoms in the field of nuclear cardiology imaging.

## Materials and methods

### Phantom design

Input image data for the phantom design were extracted from an  $^{18}\text{F}$ -FDG PET/CT study of a patient (age: 67 years; weight: 63 kg) without known coronary artery disease. Whole body PET/CT acquisition was performed on a GE Discovery MI system,

using the local patient examination protocol (injected dose 220 MBq, 1.5 min acquisition time per bed position, 30% overlap between bed positions). Q.Clear reconstruction was applied with  $384 \times 384$  matrix resulting in  $1.82 \times 1.82 \times 2.79$  mm voxel size (Fig. 1 upper row). The local ethics committee approved the use of patient data in this study.

For image segmentation process, we used the 3D Slicer software with basic functionality [30]. Images were cropped near to the area of the heart. Segmentation was done by applying the Otsu method with minimum and maximum threshold values obtained by visual inspection [31]. Irrelevant segmented voxels were deleted manually using the Erase tool. The 3D mask was saved in Standard Tessellation Language (STL) format with LPS (Left, Posterior, Superior) coordinate system and size scale of 1.0. The exported model was post-processing using Autodesk Meshmixer (Autodesk Inc., San Rafael, California, USA). The Plane Cut tool was used to make a plane surface on the left ventricle model from the direction of the left atrium perpendicular to the apex. A 0.5 mm offset distance was defined to create the model hollow, while solid accuracy and mesh density parameters were set to 512 in the Hollow tool. The size of the plain surface of the model was increased with the Extrude tool to make a 10 mm wide solid pedestal. In addition, with the Hollow and Extrude tools, a bubble trap was created. A phantom holder was also created in Trimble SketchUp Pro 2020 (Trimble Inc., Sunnyvale, California, USA) based on the distance and size of the pedestal holes of the commercially available Biodex Cardiac insert. This holder was merged with the previously created plane surface of the cardiac model in Meshmixer using Boolean Union method (Fig. 1). As a last step, two filling holes were designed, one of them through the bubble trap. Finally, with our primary purpose, two types of phantom models were designed: one as a representation of the healthy LVm with  $190 \pm 1$  ml fillable volume (Fig. 1 lower row), and another mimicking transmural

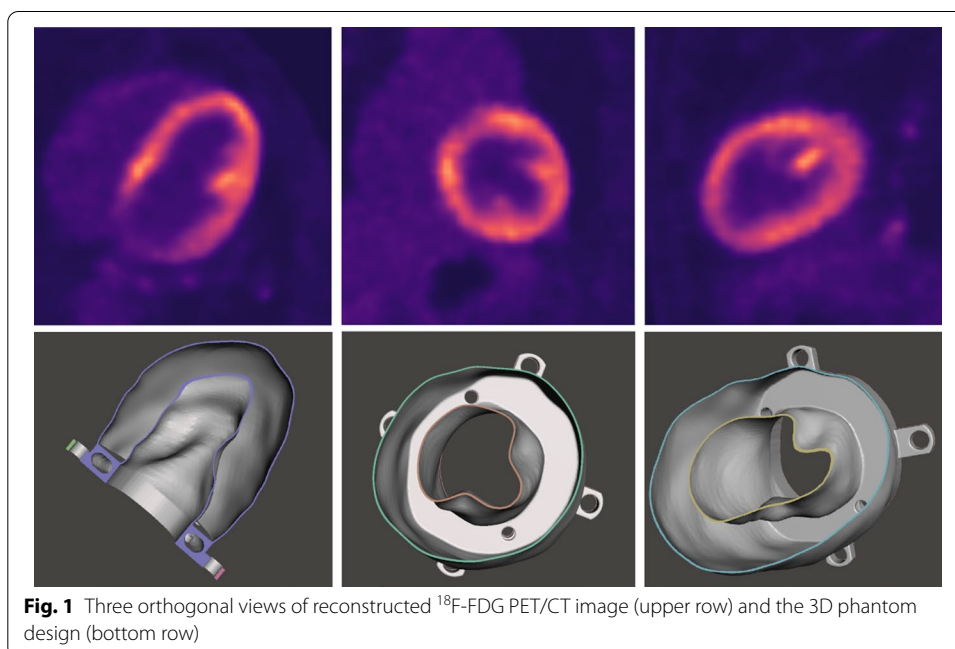


**Fig. 1** Three orthogonal views of reconstructed  $^{18}\text{F}$ -FDG PET/CT image (upper row) and the 3D phantom design (bottom row)



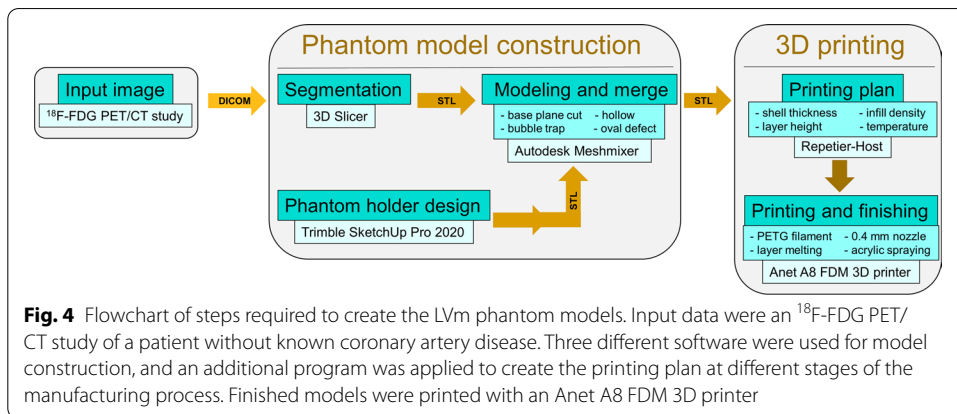
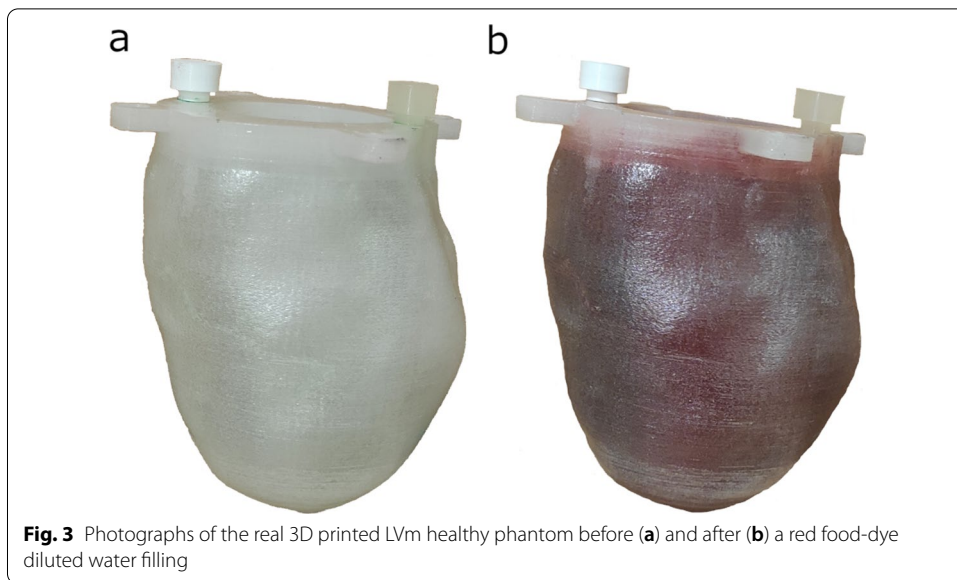
**Fig. 2** Multi-sectional image of the real 3D printed LVm defective phantom

perfusion defective myocardium with a  $20 \times 30$  mm oval solid plastic cold part (Fig. 2). The latter model has  $165 \pm 1$  ml total fillable volume. These two phantoms will be referred to in the following as LVm healthy and LVm defective phantom.

### 3D printing

For slicing and creating the print plan, the Repetier-Host (Hot-World GmbH & Co. KG, Willich, Germany) software was used. The model was laid flat on its pedestal. Slicing parameters were the followings: 100% infill density; shell thickness was 0.4 mm with 0.2 mm layer height. No adhesion or support was generated for the 40 mm/s print speed. Retraction and cooling were enabled. Phantoms were printed using an Anet A8 FDM 3D printer (Anet Technology Co., Ltd., Shenzhen, People's Republic of China), build volume  $220 \times 220 \times 240$  mm, Marlin firmware, 0.4 mm nozzle diameter, with 3DJAKE PETG transparent filament. PETG thermoplastic was used for watertight and durability reasons and to avoid significant stringing, which is a well-known phenomenon in the case of other printing materials (e.g., PLA) [32]. Print bed and nozzle temperature were set to the mid-value of the manufacturer's recommended temperature ranges: 70 °C and 240 °C, respectively. The total 3D printing time was approximately 6 h for each model. The 0.4 mm nozzle diameter and 0.4 mm shell thickness print parameter give 0.4 mm real wall thickness to the printed phantoms. A few times, the phantom had clearly visible separate layers on the outer apex side after printing, in these cases, we used a soldering iron to melt them together. To prevent any further leakage between layers, Prisma Color Acrylic spray was applied to the outer surface on the printed phantoms as a finishing process. To assure as less leaking as possible, M5 size screws were 3D printed to tightly fit in the phantom filling holes (Fig. 3).

The described steps required to create LVm phantom models are shown in Fig. 4. Our 3D phantom model is available in STL format in the supplementary material.



**Printing reproducibility, leaking test**

Reproducibility of the phantom production was demonstrated with three separate printing series. Size, including the diameter of the pedestal and filling holes, was measured with a sliding calliper. Spiral CT scans with 120 kV, 120 mA x-ray settings, and voxel size of 0.625 × 0.703 × 0.703 mm were performed and evaluated on healthy phantoms filled with water to measure the accuracy of reproducibility. For the leakage test, watertight fillings were checked at least two times for each phantom (Fig. 3).

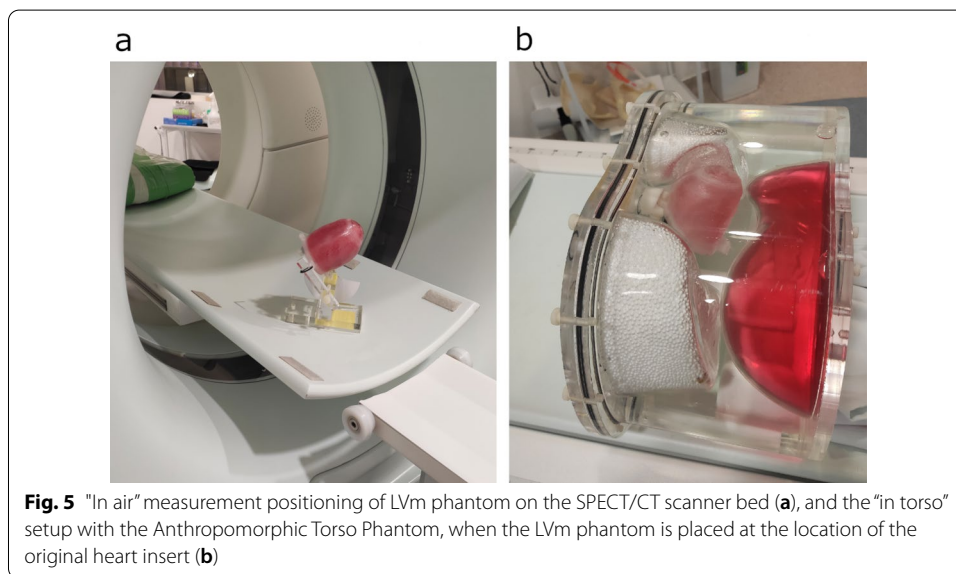
**Phantom SPECT/CT measurements**

<sup>99m</sup>Tc- water solution was mixed with red food-dye for better visual detection of bubbles and leakage. Decay corrected activity concentrations calculated to the acquisition start can be seen in Table 1.

**Table 1** Decay corrected activity concentrations in kBq/ml applied for phantom preparations

Measurement type	Volume [ml]	Activity concentrations (kBq/ml)		
		"in air"		"in torso"
Background	10100	–	–	20.15
Liver	1200	–	–	62.45
LVm healthy phantom	190	72.74	–	59.8
LVm defective phantom	165	–	69.04	–

In the first experiments, LVm healthy and defective phantoms were measured without additional scattering media ("in air"). The LVm healthy insert was also placed into the Anthropomorphic Torso Phantom for a second acquisition ("in torso")



**Measurements and reconstructions**

Both LVm healthy and LVm defective phantoms were measured without additional scattering media (referring to as "in air" measurement). The LVm healthy insert was placed into the Anthropomorphic Torso Phantom for a second acquisition (referring to as "in torso" measurement). All imaging acquisitions were performed with identical acquisition parameters on a NaI(Tl) detector-based AnyScan® DUO FLEX SPECT/CT system (Mediso Medical Imaging Systems, Budapest, Hungary) equipped with Low energy High-Resolution (LEHR) parallel hole collimator. The different phantom arrangements on the SPECT/CT scanner bed can be seen in Fig. 5. The routine clinical patient protocol for myocardial perfusion was selected, including the following parameters: 90 degrees scan arc, 64 projections, 128 × 128 matrix size, 140.5 keV energy with 20% window width, body contouring, and step and shoot mode. Additionally, a CT scan with 120 kV, 50 mA x-ray settings, and a voxel size of 2.50 × 0.977 × 0.977 mm was performed for attenuation correction purposes.

**Data processing**

Data were processed by the Mediso InterView™ XP application. Default Cardiac Perfusion Image reconstruction of Tera-Tomo™ 3D SPECT-Q was applied on the acquired

raw data. Image size of  $128 \times 128$  with 5.91 mm cubic reconstruction voxel size, 32 number of iterations and 4 subset size was used with CT-based attenuation and scatter correction. Polar maps with 17 segments were created for all three measurements and were applied to reveal similarities and differences. For this process, reorientations were performed by a medical expert physician with six years of experience. Polar maps of "in air" measurements of the healthy and defective myocardium phantoms were compared, to demonstrate how the defect alters the internal distribution of the radioactive solution inside the phantom. Since the "in torso" measurement represents more realistic scattering and attenuation conditions, the polar map of the "in air" measurement of the healthy myocardium phantom was compared to the polar map of the "in torso" measurement. Polar map graphs from the calculated percentage differences were also created for these evaluations.

## Results

After rigid registration of the high-resolution CT images of LVM healthy models, the phantoms present identical geometry within tight tolerances in shape (Fig. 6) and fillable volume.

The measured mean filled volume was  $189.4 \text{ ml} \pm 1.4 \text{ ml}$ , including the volume of the bubble trap. The printed LVM phantoms were easily refillable and were closed tightly, without any air bubbles or observable leakage during all of the presented measurements. Additionally, two phantoms were filled and stored for three months at room temperature, and no leakage or evaporation was detected. Reconstructed SPECT images of "in air" measurements reveal accurate uptake volumes (Fig. 7). Differences between defective and healthy phantom images were clearly visible on the sagittal views (Fig. 7a, b) as well as on the 3D rendered image (Fig. 7c, d). The defect appeared where it was planned during the phantom design.

Printed phantoms were compatible with the Anthropomorphic Torso Phantom to be assembled at the cardiac region. The reconstructed SPECT images revealed that the activity distribution of the LVM healthy phantom could be visualized in detail (Fig. 8).

Clear differences were found while analyzing the resulted polar maps of the three measurements of the "in air" and "in torso" arrangements (Fig. 9).

The polar map segment with the highest signal was found to be the basal anterolateral for LVM healthy and LVM defective "in air" measurements. On the other hand, the originally high signal mid-inferior region on the LVM healthy model was decreased significantly due to the artificial defect on the LVM defective model.

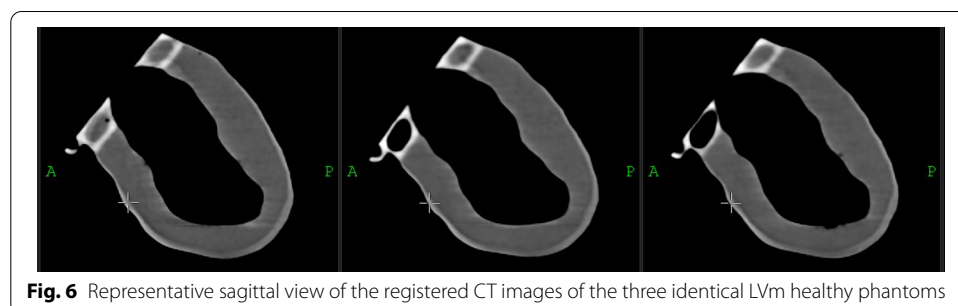
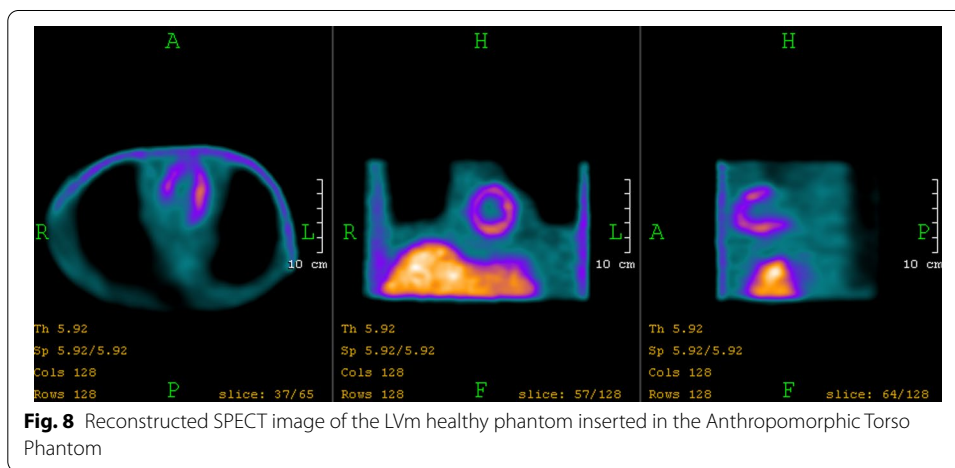
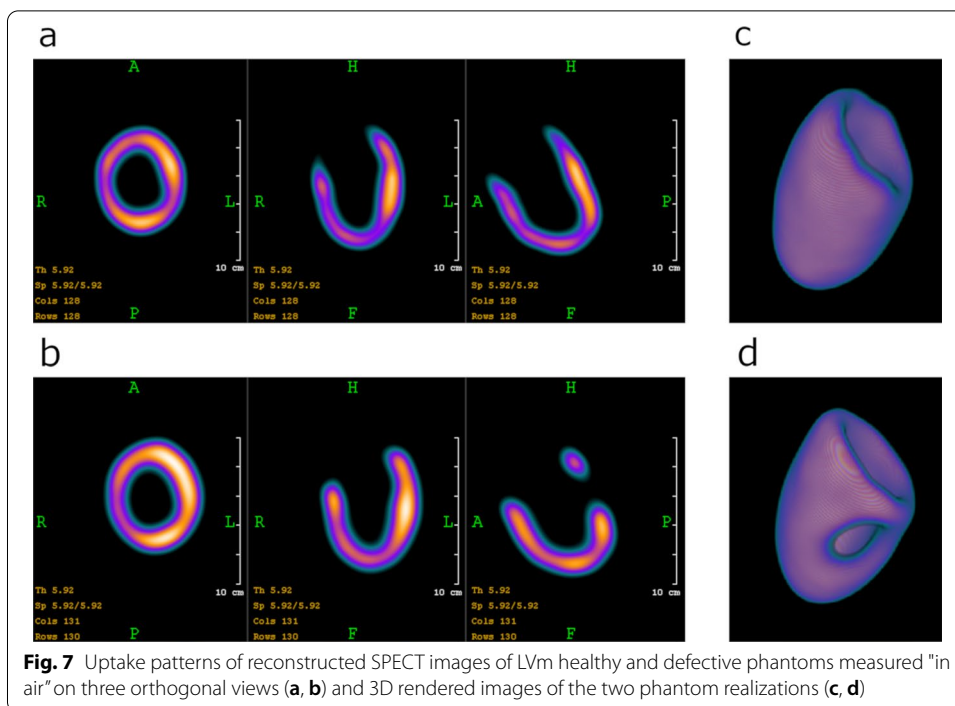


**Fig. 6** Representative sagittal view of the registered CT images of the three identical LVM healthy phantoms



Polar map segment differences of the LVM healthy phantom measurements (first and last rows in Fig. 9) could originate from at least two sources. The radiopharmaceutical activity decayed compared to the "in air" case; therefore, the overall signal yield was expectedly lower. Moreover, the liver and the background in the torso phantom contained image distortions due to the spillover effect. All three polar maps have similar apex and apical region values.

The detailed relative perfusion percentage values of each region for all three measurements are summarized in Table 2, together with the relative percentage difference of measurement comparisons.



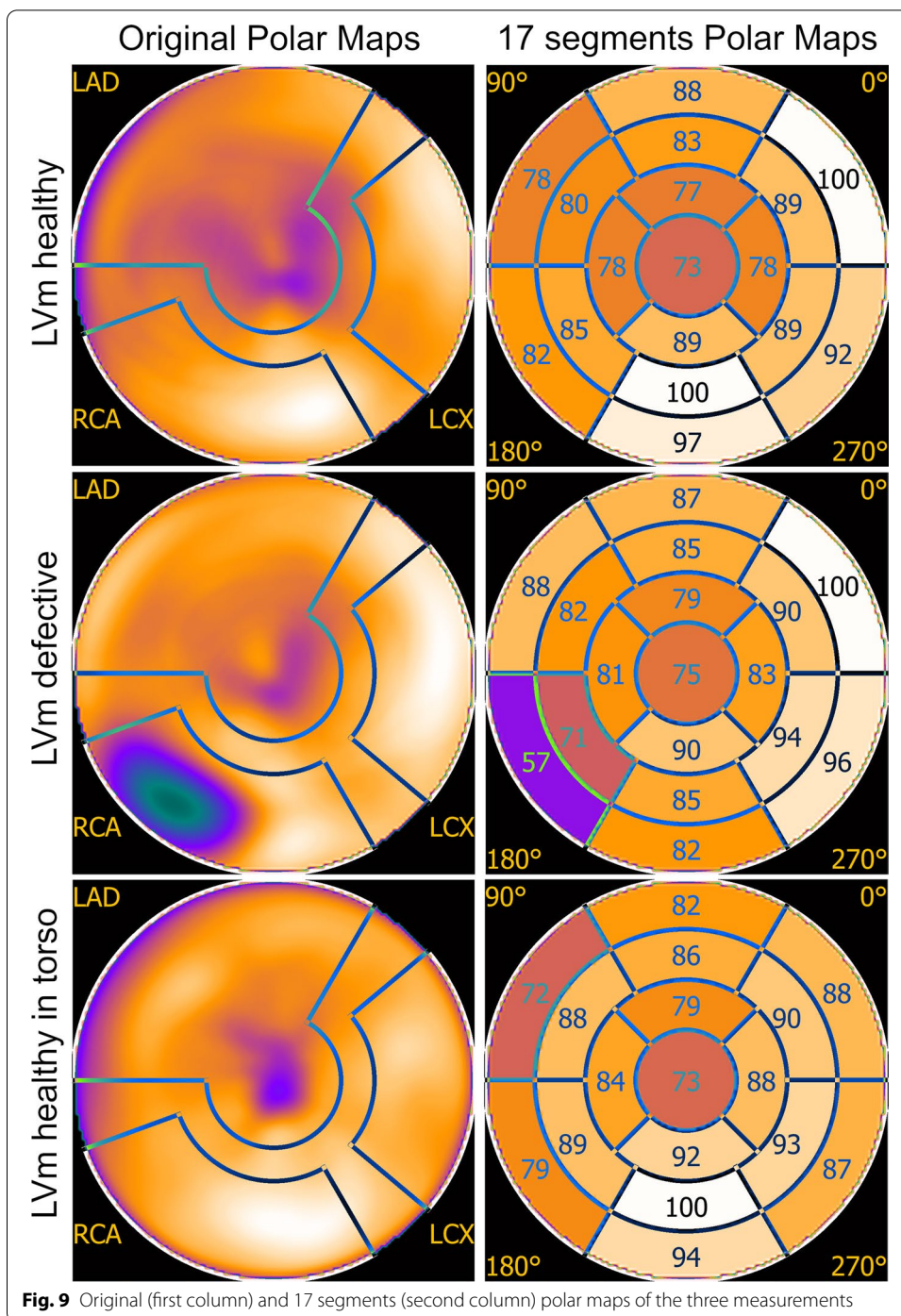


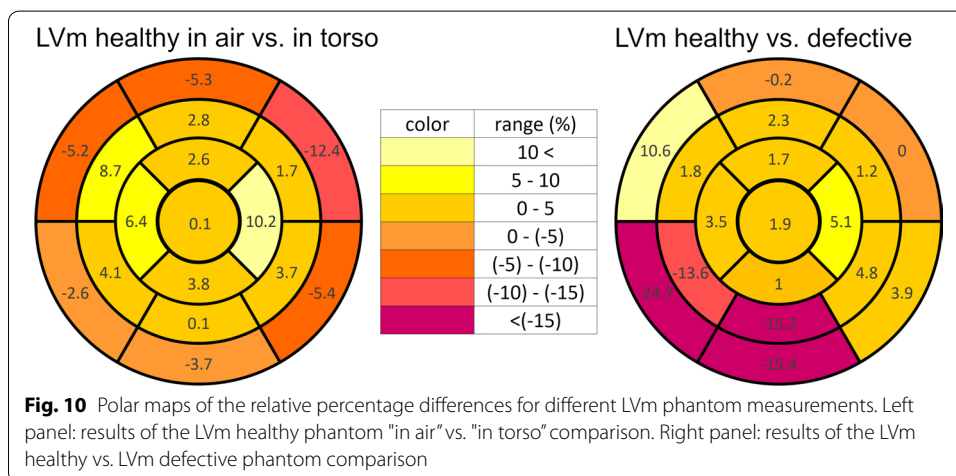
**Fig. 9** Original (first column) and 17 segments (second column) polar maps of the three measurements

In the relative % difference columns (column IV. and V.), negative value means deterioration, while a positive represents an improved region. The values of the LVm healthy—LVm defective phantom comparison (column IV.), are in the range between  $-24.7\%$  and  $10.6\%$ , and 11 of the 17 segments have less than 5% value. The LVm healthy phantom "in air"—"in torso" comparison (column V.) has values between  $-12.4\%$ , and  $10.2\%$ , and 10 of the 17 segments have values less than 5%. The relative percentage differences were

**Table 2** Polar map values for each measurement and related percentage differences

Area	I. LVm healthy phantom "in air" (%)	II. LVm defective phantom "in air" (%)	III. LVm healthy phantom "in torso" (%)	IV. Relative % difference of I. and II	V. Relative % difference of I. and III
Basal anterior	87.5	87.3	82.2	-0.2	-5.3
Basal anteroseptal	77.6	88.2	72.4	10.6	-5.2
Basal inferoseptal	82.0	57.3	79.4	-24.7	-2.6
Basal inferior	97.2	81.8	93.5	-15.4	-3.7
Basal inferolateral	92.0	95.9	86.6	3.9	-5.4
Basal anterolateral	100.0	100.0	87.6	0.0	-12.4
Mid-anterior	83.0	85.3	85.8	2.3	2.8
Mid-anteroseptal	79.7	81.5	88.4	1.8	8.7
Mid-inferoseptal	84.8	71.2	88.9	-13.6	4.1
Mid-inferior	99.9	84.7	100.0	-15.2	0.1
Mid-inferolateral	89.1	93.9	92.8	4.8	3.7
Mid-anterolateral	88.8	90.0	90.5	1.2	1.7
Apical anterior	76.9	78.6	79.5	1.7	2.6
Apical septal	77.6	81.1	84.0	3.5	6.4
Apical inferior	88.6	89.6	92.4	1.0	3.8
Apical lateral	78.3	83.4	88.5	5.1	10.2
Apex	73.1	75.0	73.2	1.9	0.1

The last two columns show the relative % difference for each segment between "in air" measurements (column I. and II.) and between the LVm healthy phantom "in air" and "in torso" measurements (column I. and III.)



also depicted on differential polar maps (Fig. 10) based on column IV. and V. values of Table 2. Each color indicates 5 percentage steps. At the LVm healthy versus LVm defective phantom comparison, the deviations were higher than 5% deterioration concentrated on the four inferior regions where the artificial defect was designed. Two regions showed an improved signal ratio of more than 5%. Improvement and relapse regions in the case of LVm healthy phantom "in air" versus "in torso" comparison did not come from the nature of our phantom. As the concerning graph shows, the deviation is located in the basal edge regions, while the values are still around 5% except for the basal

anterolateral region. This result and the 10.2% improvement in the apical region can be attributed to the uncertainty of the manual heart reorientation.

## Discussion

While several conventional plastic phantoms are available to test the image quality and reliability of nuclear cardiology applications with SPECT [8, 33–35], they still have some anatomical and size limitations. 3D printing technology has gained wide attention recently for creating anthropomorphic phantoms, due to its cost-effectiveness, fast production capability and the possibility for advanced and customized design in almost any shape even for nuclear cardiology applications [28, 29]. In this work, two anatomically accurate LV myocardial phantom inserts were created from a real patient  $^{18}\text{F}$ -FDG PET/CT study image set (Fig. 1 upper row). One represents the original healthy LV myocardium (Fig. 1 lower row), and the other includes an artificially added myocardium deficit (Fig. 2). Three LVm healthy phantoms were 3D printed to verify that there are no significant alterations in geometry (Fig. 6.) and fillable volume ( $189.4 \text{ ml} \pm 1.4 \text{ ml}$ ). These phantom inserts were planned to be convenient and complementary solutions to the commercially available plastic phantoms used in nuclear cardiology. Bubbles in the myocardium volume of the LV phantoms could affect the distribution of the radioactive solution. The LV insert of the Anthropomorphic Torso Phantom has no bubble trap, while the 3D printed LVm inserts were designed to include one for bubble-free filling of the LV wall. Therefore, the imaging of our phantoms was not affected by the presence of bubbles in the artificial myocardium volume. Moreover, the conventional LV insert is available at a certain size in a geometrically simple shape [33]; however, our 3D printed LVm insert is scalable in size and results in a more realistic uptake pattern of the LV myocardial perfusion SPECT image (Fig. 7). The latter has particularly high significance in the case of testing optimal settings for image reconstruction algorithms to avoid artifacts. The LV myocardium wall has a significantly different cross-sectional diameter at the apex than other regions, and the iterative image reconstruction tends to reach accurate activity levels at different iteration numbers for the apex than to the LV walls [36] even in case of a geometrically simple LV phantom. This is more prominent when we consider the real anatomy of the LV with non-uniform wall thickness. Therefore, our phantom design is a good advocate to the geometrically simple LV phantoms to find optimal iteration number for a certain image reconstruction. In addition, the reduction in left ventricular apical tracer uptake called apical thinning or false apical defect [37] is frequently observed in myocardial perfusion imaging both in the field of PET [38] and SPECT imaging [39, 40]. Among many potential causes, the diminished activity at the apex can be attributed to real anatomy [41] combined with the partial volume effect, as it is visible in our phantom model as well (Fig. 6). Another commercially available phantom called the Kyoto HL cardiac torso phantom (Kyoto Kagaku Co. Ltd., Kyoto, Japan) was used by Yoneyama et al. to test image reconstruction resolution recovery solutions to overcome ejection fraction (EF) limitations in case of pediatric patients [42]. However, with our method, two small size hearts can be printed from normal gated PET image sets in end-systole and end-diastole phases, and the EF measurement accuracy of different reconstruction methods can be tested [43]. It has to be mentioned that the commercially available AGATE phantom [8] can mimic simple heart motion and is

compatible with the Anthropomorphic Torso Phantom. Therefore, gated SPECT acquisitions and EF calculation are possible; however, this phantom is also available only in adult patient size. The anatomically correct design of the LV myocardium is also important when comparing hybrid or ellipsoid sampling of polar map generation [44]. A set of printed phantoms with different clinically representative cases could be used to perform a comparison of existing nuclear cardiology software, since considerable differences are present in their performance [45]. We performed a representative set of SPECT image acquisitions using the 3D printed phantom inserts. Both LVm healthy and LVm perfusion defect phantoms were filled with  $^{99m}\text{Tc}$ , and SPECT acquisitions were performed on an AnyScan<sup>®</sup> DUO FLEX SPECT/CT system "in air", without any scattering media and in the Anthropomorphic Torso Phantom including hot background and hot liver insert. The printed LVm models remained intact throughout the experiments, and the inserted  $^{99m}\text{Tc}$  radioactive solution did not dissolve into the torso phantom background chamber. Seventeen segments polar map analysis of SPECT images revealed that by comparing the LVm defective model to the LVm healthy one, a significant deficit in the radiopharmaceutical distribution appeared where it was expected (Fig. 9). The design process enables flexibility in placing the perfusion deficit with different numbers and shapes within the fillable wall of the phantom. Including the expected low perfusion segments at the deficit area, around 65% of the polar map segments had less than 5% deviation. When comparing the LVm healthy model, the "in torso" and "in air" measurements, 59% of all polar map segments had less than 5% deviation (Fig. 10). Concerning only the segments excluding the deficit area, neither comparison revealed more than 12.4% deviation, which difference could have originated most probably from phantom positioning error, the applied reconstruction method, and the well-known spill-over effect, especially in the case of the "in torso" phantom measurement. Beyond the flexibility and applicability of our method, this study has several limitations. We used an  $^{18}\text{F}$ -FDG PET image set to create the phantom model; however, a more realistic model can be created with currently available PET myocardial perfusion traces such as  $^{82}\text{Rb}$ -chloride,  $^{13}\text{N}$ -ammonia or  $^{18}\text{F}$ -flurpiridaz. We presented 3D printed phantoms in one LV size from a non-gated PET data of a healthy male patient. It would be beneficial to demonstrate phantom studies using healthy females and pediatric or even heart disease images as input data. On the other hand, the variety of these printable LVm phantoms should be limited to provide a few standardized shapes available to be downloaded and printed in any nuclear cardiology laboratory. The LV deficit designed and printed in the phantom was completely solid, representing scar burden. However, a fillable defect could be printed within the LV wall, and lower activity concentration can be inserted in that chamber to mimic ischemia. In this study, only the LV was segmented; however, the anthropomorphic nature of the phantom could be emphasized with a model including the right ventricle as well.

## Conclusion

In this study, we proved that creating a fillable, anthropomorphic 3D printed phantom of the LV myocardium segmented from a real patient PET image volume is possible. SPECT images were acquired in different imaging scenarios proving the usefulness of the printed LVm phantoms. The flexibility of the 3D printing process presented in this

study provides scalable and anthropomorphic image quality phantoms in nuclear cardiology imaging.

#### Abbreviations

DLP: Digital light processing; EF: Ejection Fraction; FDM: Fused deposition modelling; LEHR: Low Energy High-Resolution; LPS: Left, Posterior, Superior; LV: Left ventricle; LVm: Left ventricle myocardium; PETG: Polyethylene terephthalate glycol; PLA: Polylactic acid; SLA: Stereo-lithography; STL: Standard Tessellation Language.

#### Acknowledgements

Not applicable.

#### Author contributions

AKK proposed the original idea, helped to find the right model design, and helped the polar map generation. LB, GT and AF helped to plan the measurements and analyzed the results from technical aspects. KK helped to complete the phantom measurements. MM analyzed the results from medical aspects. JK segmented, CAD designed, and 3D printed the presented LVm models as well as contributed to the measurements and wrote the manuscript draft. All authors read and approved the final manuscript.

#### Funding

Open access funding provided by University of Debrecen. The research was supported by the Thematic Excellence Programme (TKP2020-NKA-04) of the Ministry for Innovation and Technology in Hungary.

#### Availability of data and materials

Our phantom inserts are available in STL format in the supplementary material.

#### Declarations

##### Ethics approval and consent to participate

The use of the  $^{18}\text{F}$ -FDG PET/CT data of the corresponding anonym patient in this study was approved by the local ethics committee.

##### Consent for publication

Not applicable.

##### Competing interests

This study was performed as part of the first author's PhD project. The other authors declare that they have no competing interests.

##### Author details

<sup>1</sup>Division of Radiology and Imaging Science, Department of Medical Imaging, Faculty of Medicine, University of Debrecen, Nagyerdei krt. 98., Debrecen 4032, Hungary. <sup>2</sup>Division of Nuclear Medicine and Translational Imaging, Department of Medical Imaging, Faculty of Medicine, University of Debrecen, Nagyerdei krt. 98., Debrecen 4032, Hungary. <sup>3</sup>ScanoMed Nuclear Medicine Centers, Nagyerdei krt. 98., Debrecen 4032, Hungary. <sup>4</sup>Mediso Ltd., Laborc Utca 3., Budapest 1037, Hungary.

Received: 14 October 2021 Accepted: 20 April 2022

Published online: 03 May 2022

#### References

1. Ryu H, Meikle SR, Willowson KP, Eslick EM, Bailey DL. Performance evaluation of quantitative SPECT/CT using NEMA NU 2 PET methodology. *Phys Med Biol*. 2019;64:145017.
2. Attarwala AA, Hardiansyah D, Romanó C, Jiménez-Franco LD, Roscher M, Wängler B, et al. Performance assessment of the ALBIRA II pre-clinical SPECT S102 system for  $^{99\text{m}}\text{Tc}$  imaging. *Ann Nucl Med*. 2021;35:111–20. <https://doi.org/10.1007/s12149-020-01547-7>.
3. Khorshidi A. Assessment of SPECT images using UHRFB and other low-energy collimators in brain study by Hoffman phantom and manufactured defects. *Eur Phys J Plus*. 2020;135:1–19. <https://doi.org/10.1140/epjp/s13360-020-00238-6>.
4. Blaire T, Bailliez A, Ben Bouallegue F, Bellevre D, Agostini D, Manrique A. First assessment of simultaneous dual isotope ( $^{123}\text{I}/^{99\text{m}}\text{Tc}$ ) cardiac SPECT on two different CZT cameras: a phantom study. *J Nucl Cardiol*. 2018;25:1692–704.
5. Timmins R, Ruddy TD, Wells RG. Patient position alters attenuation effects in multipinhole cardiac SPECT. *Med Phys*. 2015;42:1233–40.
6. Zhang D, Ghaly M, Mok GSP. Interpolated CT for attenuation correction on respiratory gating cardiac SPECT/CT—a simulation study. *Med Phys*. 2019;46:2621–8.
7. Veress AI, Fung GSK, Lee TS, Tsui BMW, Kicska GA, Segars WP, et al. The direct incorporation of perfusion defect information to define ischemia and infarction in a finite element model of the left ventricle. *J Biomech Eng*. 2015;137:1–10.

8. Visser JJJ, Sokole EB, Verberne HJ, Habraken JBA, Van De Stadt HJF, Jaspers JEN, et al. A realistic 3-D gated cardiac phantom for quality control of gated myocardial perfusion SPET: the Amsterdam gated (AGATE) cardiac phantom. *Eur J Nucl Med Mol Imaging*. 2004;31:222–8.
9. Kim S, Oh J, Jeong D, Park W, Bae J. Consistent and reproducible direct ink writing of eutectic gallium-indium for high-quality soft sensors. *Soft Robot*. 2018;5:601–12.
10. Abdullah KA, McEntee MF, Reed W, Kench PL. Development of an organ-specific insert phantom generated using a 3D printer for investigations of cardiac computed tomography protocols. *J Med Radiat Sci*. 2018;65:175–83.
11. Okkalidis N, Chatzigeorgiou C, Okkalides D. Assessment of 11 available materials with custom three-dimensional-printing patterns for the simulation of muscle, fat, and lung hounsfield units in patient-specific phantoms. *J Eng Sci Med Diagn Ther*. 2018;1:1–7.
12. Vyavahare S, Teraiya S, Panghal D, Kumar S. Fused deposition modelling: a review. *Rapid Prototyp J*. 2020;26:176–201.
13. Hong D, Lee S, Kim GB, Lee SM, Kim N, Seo JB. Development of a CT imaging phantom of anthropomorphic lung using fused deposition modeling 3D printing. *Medicine (United States)*. 2020;99:e18617.
14. Zhang J, Hu Q, Wang S, Tao J, Gou M. Digital light processing based three-dimensional printing for medical applications. *Int J Bioprinting*. 2020;6:12–27.
15. Robinson SS, Aubin CA, Wallin TJ, Gharai S, Xu PA, Wang K, et al. Stereolithography for personalized left atrial appendage occluders. *Adv Mater Technol*. 2018;3:1–9.
16. Ramírez-Nava GJ, Santos-Cuevas CL, Chairez-Oria I, Rioja-Guerrero E, Oroz-Duarte J. Tomographic  $^{99m}\text{Tc}$  radioactivity quantification in three-dimensional printed polymeric phantoms with bioinspired geometries. *Radiat Phys Chem*. 2020;177:109130. <https://doi.org/10.1016/j.radphyschem.2020.109130>.
17. Gear JI, Cummings C, Craig AJ, Divoli A, Long CDC, Tapner M, et al. Abdo-Man: a 3D-printed anthropomorphic phantom for validating quantitative SIRT. *EJNMMI Phys*. 2016. <https://doi.org/10.1186/s40658-016-0151-6>.
18. Anwari V, Lai A, Ursani A, Rego K, Karasfi B, Sajja S, et al. 3D printed CT-based abdominal structure mannequin for enabling research. *3D Print Med*. 2020. <https://doi.org/10.1186/s41205-020-0056-9>.
19. Alqahtani MS, Lees JE, Bugby SL, Samara-Ratna P, Ng AH, Perkins AC. Design and implementation of a prototype head and neck phantom for the performance evaluation of gamma imaging systems. *EJNMMI Phys*. 2017. <https://doi.org/10.1186/s40658-017-0186-3>.
20. Woliner-van der Weg W, Deden LN, Meeuwis APW, Koenrades M, Peeters LHC, Kuipers H, et al. A 3D-printed anatomical pancreas and kidney phantom for optimizing SPECT/CT reconstruction settings in beta cell imaging using  $^{111}\text{In}$ -exendin. *EJNMMI Phys*. 2016. <https://doi.org/10.1186/s40658-016-0165-0>.
21. Gear JI, Cummings C, Sullivan J, Cooper-Rayner N, Downs P, Murray I. Radioactive 3D printing for the production of molecular imaging phantoms. *Phys Med Biol*. 2020. <https://doi.org/10.1088/1361-6560/aba40e>.
22. Lämpchen T, Meier LP, Fürstner M, Prenosil GA, Krause T, Rominger A, et al. 3D printing of radioactive phantoms for nuclear medicine imaging. *EJNMMI Phys*. 2020. <https://doi.org/10.1186/s40658-020-00292-0>.
23. Robinson AP, Tipping J, Cullen DM, Hamilton D, Brown R, Flynn A, et al. Organ-specific spect activity calibration using 3d printed phantoms for molecular radiotherapy dosimetry. *EJNMMI Phys*. 2016;3:1–11. <https://doi.org/10.1186/s40658-016-0148-1>.
24. Filippou V, Tsoumpas C. Recent advances on the development of phantoms using 3D printing for imaging with CT, MRI, PET, SPECT, and ultrasound. *Med Phys*. 2018;45:e740–60.
25. Gear JI, Long C, Rushforth D, Chittenden SJ, Cummings C, Flux GD. Development of patient-specific molecular imaging phantoms using a 3D printer. *Med Phys*. 2014;41:1–4.
26. Tran-Gia J, Lassmann M. Optimizing image quantification for  $^{177}\text{Lu}$  SPECT/CT based on a 3D printed 2-compartment kidney phantom. *J Nucl Med*. 2018;59:616–24.
27. Pfaehler E, Beukinga RJ, de Jong JR, Slart RHJA, Slump CH, Dierckx RAJO, et al. Repeatability of  $^{18}\text{F}$ -FDG PET radiomic features: a phantom study to explore sensitivity to image reconstruction settings, noise, and delineation method. *Med Phys*. 2019;46:665–78.
28. Matsutomo N, Seki H, Hishikawa M, Motegi K, Yamamoto T. Technical Note: development of an ischemic defect model insert attachable to a commercially available myocardial phantom. *Med Phys*. 2020;47:4340–7.
29. Green S, Grice J. Technical note: 3D-printed phantom for dedicated cardiac protocols and geometries in nuclear medicine. *Med Phys*. 2021. <https://doi.org/10.1002/mp.15406>.
30. Fedorov A, Beichel R, Kalpathy-Cramer J, Finet J, Fillion-Robin JC, Pujol S, et al. 3D Slicer as an image computing platform for the Quantitative Imaging Network. *Magn Reson Imaging*. 2012;30:1323–41. <https://doi.org/10.1016/j.mri.2012.05.001>.
31. Liu D, Yu J. Otsu method and K-means. In: *Proceedings of 2009 9th Int Conf Hybrid Intell Syst HIS 2009*, vol. 1. 2009. p. 344–9.
32. Paraskevoudis K, Karayannis P, Koumoulos EP. Real-time 3D printing remote defect detection (stringing) with computer vision and artificial intelligence. *Processes*. 2020;8:1464.
33. Imbert L, Poussier S, Franken PR, Songy B, Verger A, Morel O, et al. Compared performance of high-sensitivity cameras dedicated to myocardial perfusion SPECT: a comprehensive analysis of phantom and human images. *J Nucl Med*. 2012;53:1897–903.
34. Liu CJ, Cheng JS, Chen YC, Huang YH, Yen RF. A performance comparison of novel cadmium–zinc–telluride camera and conventional SPECT/CT using anthropomorphic torso phantom and water bags to simulate soft tissue and breast attenuation. *Ann Nucl Med*. 2015;29:342–50. <https://doi.org/10.1007/s12149-015-0952-z>.
35. Kobayashi H, Momose M, Kanaya S, Kondo C, Kusakabe K, Mitsuhashi N. Scatter correction by two-window method standardizes cardiac  $^{123}\text{I}$ -MIBG uptake in various gamma camera systems. *Ann Nucl Med*. 2003;17:309–13.
36. Okuda K, Nakajima K, Yoneyama H, Shibutani T, Onoguchi M, Matsuo S, et al. Impact of iterative reconstruction with resolution recovery in myocardial perfusion SPECT: phantom and clinical studies. *Sci Rep*. 2019;9:1–9. <https://doi.org/10.1038/s41598-019-56097-4>.
37. Purser NJ, Armstrong IS, Williams HA, Tonge CM, Lawson RS. Apical thinning: real or artefact? *Nucl Med Commun*. 2008;29:382–9.

38. Steffen DA, Giannopoulos AA, Grossmann M, Messerli M, Schwyzer M, Gräni C, et al. "Apical thinning": relations between myocardial wall thickness and apical left ventricular tracer uptake as assessed with positron emission tomography myocardial perfusion imaging. *J Nucl Cardiol*. 2020;27:452–60.
39. Denisova NV, Ansheles AA. A study of false apical defects in myocardial perfusion imaging with SPECT/CT. *Biomed Phys Eng Express*. 2018. <https://doi.org/10.1088/2057-1976/aae414>.
40. Okuda K, Nakajima K, Matsuo S, Kondo C, Sarai M, Horiguchi Y, et al. Creation and characterization of normal myocardial perfusion imaging databases using the IQ-SPECT system. *J Nucl Cardiol*. 2018;25:1328–37.
41. Johnson KM, Johnson HE, Dowe DA. Left ventricular apical thinning as normal anatomy. *J Comput Assist Tomogr*. 2009;33:334–7.
42. Yoneyama H, Nakajima K, Okuda K, Matsuo S, Onoguchi M, Kinuya S, et al. Reducing the small-heart effect in pediatric gated myocardial perfusion single-photon emission computed tomography. *J Nucl Cardiol*. 2017;24:1378–88.
43. Germano G, Kavanagh PB. Ready, shoot, aim? Summary justice for small hearts in nuclear cardiology. *J Nucl Cardiol*. 2017;24:1389–92.
44. Germano G, Kavanagh PB, Waechter P, Areeda J, Van Kriekinge S, Sharir T, et al. A new algorithm for the quantitation of myocardial perfusion. SPECT I: technical principles and reproducibility. *J Nucl Med*. 2000;41:712–9.
45. Johansson L, Lomsky M, Marving J, Ohlsson M, Svensson SE, Edenbrandt L. Diagnostic evaluation of three cardiac software packages using a consecutive group of patients. *EJNMMI Res*. 2011;1:1–7.

### Publisher's Note

Springer Nature remains neutral with regard to jurisdictional claims in published maps and institutional affiliations.

**Submit your manuscript to a SpringerOpen<sup>®</sup> journal and benefit from:**

- ▶ Convenient online submission
- ▶ Rigorous peer review
- ▶ Open access: articles freely available online
- ▶ High visibility within the field
- ▶ Retaining the copyright to your article

---

Submit your next manuscript at ▶ [springeropen.com](https://www.springeropen.com)

---